Dynamic Temperature Prediction of the Magnetic Coupler in Wireless Charging Systems

Xianzhen Li, Zhenjie Li, *Member, IEEE*, Dechun Yuan, Yabiao Zhao, Mingfei Ban, *Member, IEEE*, and Yiqi Liu, *Member, IEEE*

***Abstract*—As the core component of wireless charging systems, the magnetic coupler usually accounts for a significant proportion of total system power losses, resulting in substantial cumulative temperature rise. This article proposes a multipoint dynamic temperature prediction method for magnetic couplers, integrating multiphysics finite-element simulation with a deep learning algorithm to achieve real-time, accurate prediction of temperature variations under ambient temperature fluctuations, coil misalignment, and continuous charging conditions. First, an electromagnetic-thermal coupled model is constructed using the finite-element method to generate temperature datasets under various operating conditions. Then, the random forest algorithm analyzed the influence of input parameters on temperature predictions at different timesteps, screening key variables as model inputs. A dynamic temperature prediction model combines long short-term memory networks with a temporal self-attention mechanism. Finally, the model outputs show that the method outperforms conventional prediction accuracy and speed approaches. Finally, a 3.3 kW experimental prototype was built to simulate continuous charging scenarios under varying coil misalignment conditions, with real-time temperature acquisition at key locations of the magnetic coupler. Experimental results show average prediction errors of 5.7%, validating the correctness of the proposed method.**

***Index Terms*—Dynamic thermal prediction, electromagnetic–thermal coupling, long short-term memory (LSTM), random forest algorithm, temporal self-attention mechanism, wireless charging system (WCS), wireless power transfer (WPT).**

I. Introduction

WIRELESS charging system (WCS) eliminates electrical hazards caused by physical contact through contactless energy transmission [1], [2], [3]. Compared to conventional wired charging methods, the WCS's contactless operation improves deployment flexibility and operational safety while eliminating connector wear and insulation degradation risks. Currently, the WCS is widely used in electric vehicles [4], [5], industrial automated guided vehicles [6], [7], and uncrewed aerial vehicles [8], [9], owing to their high efficiency and flexibility. Under actual operating conditions, it is necessary to conduct further research on the cumulative temperature rise problem that occurs when the WCS operates for a long time [10], [11], [12].

On one hand, the magnetic coupler is the core component of WCS, accounting for a significant portion of the system's power losses during energy transfer. On the other hand, losses are converted into heat, leading to a cumulative temperature rise, directly impacting the system's reliability and safety. Excessive temperatures accelerate the material degradation and increase the risk of thermal failure. Thermal monitoring is essential to control the temperature of the magnetic coupler within a safe operating range. Therefore, an accurate real-time temperature prediction method for the magnetic coupler is crucial for practical applications, which is just the research background of this article.

A. Existing Relevant Research Works

The methods for the magnetic coupler's thermal analysis and hotspot temperature can be divided into two conventional methods: the thermal network method (TNM) and the finite-element method (FEM).

TNM analyzes the temperature distribution through thermal resistance networks, typically achieved by establishing an electrical circuit analogy of heat transfer processes in the magnetic coupler. This method calculates hotspot temperature distributions through nodal thermal analysis, employing heat transfer theory and thermal-electrical analogy principles. An equivalent thermal network is built to analyse heat conduction and dissipation in the magnetic coupler, which qualitatively characterizes temperature distributions of the coupler [14]. In [15], an improved thermal model for liquid-cooled magnetic couplers was developed using a thermal network to analyse the thermally critical components' temperature distribution and heat transfer pathways. This enables the accurate prediction of steady-state thermal behavior. Delgado et al. [16] present a 3D thermal model for coils based on high-granularity 2D-thermal networks, enabling rapid simulation and analysis of the thermal characteristics. In [17], an equivalent thermal network model is constructed using the lumped method to characterize magnetic couplers under natural convection conditions. The maximum

Received 5 August 2025; revised 21 October 2025; accepted 29 November 2025. Date of publication 5 December 2025; date of current version 25 February 2026. This work was supported in part by the Fundamental Research Funds for the Central Universities under Grant 2572025JT02, in part by the Fundamental Research Funds for the Central Universities under Grant 2572023CT15, in part by the China Postdoctoral Science Foundation under Grant 2022M710641, and in part by the National Natural Science Foundation of China under Grant 52107001. Recommended for publication by Associate Editor M. Ponce-Silva. *(Corresponding author: Zhenjie Li.)*

The authors are with the College of Computer and Control Engineering, Northeast Forestry University, Harbin 150040, China (e-mail: lixianzhen23@nefu.edu.cn; lizhenjie0725@nefu.edu.cn; 15114558998@nefu.edu.cn; zyb0129@nefu.edu.cn; banmingfei@nefu.edu.cn; nefukzch@nefu.edu.cn).

Color versions of one or more figures in this article are available at https://doi.org/10.1109/TPEL.2025.3640679.

Digital Object Identifier 10.1109/TPEL.2025.3640679

internal temperature is predicted based on losses, dimensions, and original operating conditions for coils with similar geometric and material properties and external thermal environments. The primary objective of the existing research on TNM is to accurately reconstruct internal heat flux pathways within the magnetic coupler through refined thermal resistance parameterisation. However, relying on limited temperature measurement points to characterize the temperature rise of magnetic couplers results in insufficient resolution. Additionally, frequent updates of model parameters are required when material properties degrade, making it inadequate for real-time temperature prediction demands.

The alternative approach uses FEM to predict temperature distributions in magnetic couplers. FEM involves constructing physical models in ANSYS, utilising coupled multiphysics simulations to predict holistic temperature profiles within the magnetic coupler [18]. In high-density compact couplers, FEM predicts steady-state temperatures and proposes thermal mitigation strategies [19]. In [20], FEM is implemented to analyse temperature distributions of enclosed WCS under real-road environmental conditions, guiding WCS design. In high-power WCS, a three-phase thermal model that distinguishes temperature behaviours is built between magnetic and nonmagnetic materials using FEA [21]. In [22], a multiobjective Pareto optimisation framework was established by integrating FEM-based thermal predictions with nondominated sorting genetic algorithm II. Although FEM provides high accuracy, its substantial hardware requirements and computational time demands critically limit its applicability in real-time thermal prediction for magnetic couplers.

The advancement of artificial intelligence (AI) algorithms has positioned them as a pivotal research focus in temperature prediction. These algorithms establish nonlinear mappings between hotspot temperatures and multiphysics parameters, significantly reducing computational complexity compared to conventional methods. Their applications in electrical equipment thermal management include extreme gradient boosting [23], genetic programming [24], and convolutional neural networks [25] for transformer dynamic thermal modelling. Improved sailfish optimizer-support vector machines for the prediction of IGBT junction temperature [26]. Nevertheless, conventional AI algorithms exhibit limited capacity in modelling long-term temporal dependencies of thermal prediction. Long short-term memory (LSTM) networks overcome this limitation through gated mechanisms, demonstrating superior performance in transformer thermal prediction. In [27], LSTM is implemented for metro transformer winding temperature forecasting by mining temporal patterns, while [28] integrated Bayesian optimisation to improve oil temperature prediction accuracy and enable fault detection. In [29], LSTM further enhances generalisation through dropout regularization and early stopping, validated with seasonal operational data. In [30], an improved LSTM model is proposed for accurate junction temperature prediction of IGBT modules.

Although AI algorithms are widely and successfully used in temperature prediction for conventional electrical equipment, the WCS exhibits unique challenges due to its dynamic operating characteristics. During practical operation, WCS experiences nonlinear fluctuations in the coupling coefficient due to position misalignment and air gap variations, which alter transmission power and significantly modify thermal distributions [10], [22], [31]. In addition, residual heat from previous charging cycles accumulates in the magnetic coupler. It superimposes with the temperature rise during subsequent charging processes, resulting in more complex transient thermal behavior than that observed in stationary electrical devices.

B. Main Works and Contributions

This article proposes a real-time temperature prediction method that couples electromagnetic-thermal simulation for data generation, random forest algorithms for key features selection, and a temporal self-attention-enhanced LSTM network for accurate time-series modeling. Combining these algorithms enhances the temperature model's prediction accuracy and efficiency. The main contributions are as follows:

1) Develop a coupled electromagnetic-thermal simulation model to generate hotspot temperature datasets for the magnetic coupler under operational conditions of coil misalignment, ambient temperature variations, and residual heat accumulation.
2) Develop a random forest feature selection method to identify strongly correlated parameters, reducing model complexity and computational time through feature importance evaluation while mitigating overfitting risks.
3) Design an LSTM network integrated with a temporal self-attention mechanism that assigns different weights to hidden states at different time steps, enabling the model to focus on critical temporal patterns to improve prediction accuracy under complex thermal conditions.

This rest of this article is organized as follows: Section II presents the principles of WCS and establishes a thermal model for the magnetic couplers. Section III generates the temperature prediction dataset and introduces the feature prioritisation method based on the random forest algorithm. Section IV elaborates on the LSTM network temperature prediction model integrated with a temporal self-attention mechanism. Section V experimentally validates prediction accuracy and real-time performance. Finally, Section VI concludes this article.

II. Theoretical and Thermal Model of the WCS

A. Structure of The WCS

Fig. 1(a) shows the magnetic coupler analyzed in this article, with its design parameters detailed in Table I.

As shown in Fig. 1, the transmitter pad is integrated into the ground-side power infrastructure, while the receiver pad is mounted on the vehicle-side pickup unit. As illustrated in the exploded view of Fig. 1(b), both transmitter and receiver employ symmetrical magnetic circuit structures. Litz wire windings are mechanically secured with hot-melt adhesive and aluminium shielding plates to suppress external magnetic flux leakage. To enhance heat transfer efficiency, silicone grease pads are applied at the coil-core and core-shielding plate interfaces. The

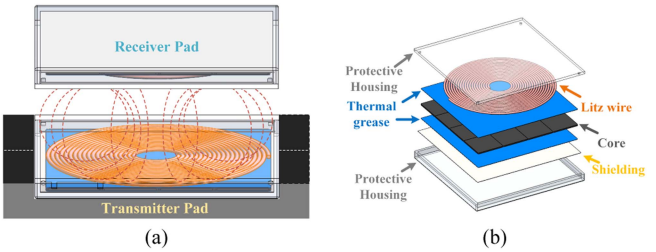

Fig. 1. (a) Magnetic coupler of the WCS system. (b) Assembly structure of the Magnetic Coupler.

TABLE I
MATERIAL AND SPECIFICATIONS OF THE WCS

Component	Type	Dimension
Litz wire	Silk-covered wire	0.05 mm × 1000
Core	Ferrite PC95	5.35 mm × 5.35 mm × 2.5 mm × 16
Shielding	Aluminum 1060	215 mm × 215 mm × 0.5 mm
Thermal grease	Silicon Pad	215 mm × 215 mm × 0.5 mm
Protective Housing	Photosensitive Resin 9400	230 mm × 230 mm × 20 mm
Coil insulation layer	Heat Shrink Tube	
Coil former	Hot Melt Adhesive	

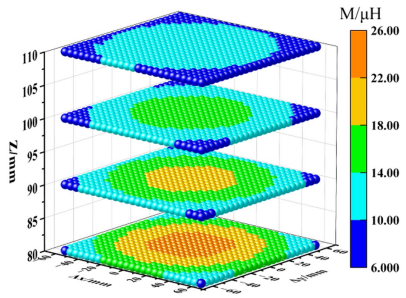

Fig. 2. Misalignment performance of different *D*.

3D-printed photosensitive resin housing protects against harsh environmental conditions like dust and moisture.

B. External Circuit Model

In practical operation, significant variations in electric vehicle chassis height inevitably cause horizontal/vertical misalignment between the receiver coil integrated into the chassis and the transmitter coil. This spatial offset modifies the mutual inductance M, inducing voltage and current fluctuations that directly degrade the thermal stability of WCS. Fig. 2 illustrates the variation in mutual inductance due to horizontal and vertical misalignment.

To further analyze the impact of this mutual inductance variation on the power transfer process, the corresponding circuit topology of the WCS is established. The WCS structure and its specifications are shown in Fig. 3 and Table II. The full-bridge inverter comprising four MOSFETs and four diodes (S_1–S_4) converts the dc input into high-frequency ac. The transmitter-side coil L_P with series compensation capacitor C_P and the receiver-side coil L_S with series capacitor C_S form a series-series compensation network through a magnetic coupler. The receiver-side

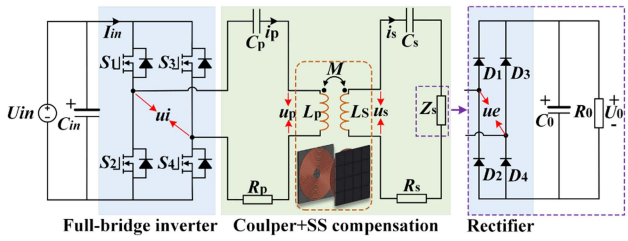

Fig. 3. Structure of the proposed WCS.

TABLE II
MAIN PARAMETERS OF THE WCS

Variable	Values	Description
P_{max}	3.3 kW	Output Power
f	85 kHz	Transmission Frequency
L_P	97 μH	Self-inductance of the transmitter coil
L_S	101 μH	Self-inductance of the receiver coil
C_P	36 nF	Compensation capacitance of the transmitter coil
C_S	35 nF	Compensation capacitance of the receiver coil

full-bridge rectifier, constructed with diodes D_1–D_4, converts the high-frequency ac into dc, which is subsequently filtered by capacitor C_0 to deliver stable power to the load R_0.

As shown in Fig. 3, u_i and ue are high-frequency square waves. Under the action of the resonant network, the currents i_p and i_s become sinusoidal. Fluctuations in mutual inductance lead to changes in transmitted power, which in turn cause variations in coil currents and voltages. These variations indirectly affect the power losses within the magnetic coupler. Therefore, it is essential to analyse the relationship between electromagnetic parameters and losses in the magnetic coupler, as discussed in the following section.

C. Temperature-Dependent Electrical Properties of Materials

1) Litz Wire: At 85 kHz, the strand diameter is significantly smaller than the skin depth, making skin-effect-induced losses negligible [32]. The total resistance, mainly consisting of proximity-effect-induced resistance R_{ind} and conduction resistance R_{con}, is expressed as

$$RLitz = Rcon + Rind = \frac{1}{\alpha_{Cu}}\left[\sum_{i=1}^{N}\frac{2r_i}{r_s^2 n_0} + \frac{n_0\pi\gamma^4}{4I^2S}\int_V H^2(x,y,z)dv\right] \quad (1)$$

$$\gamma = r_s\sqrt{\mu_0\mu_{Cu}\alpha_{Cu}\omega} \quad (2)$$

where N is the number of parallel branches, r_i is the radius of a single Litz strand, r_s is the radius of the bundled strands, n_0 is the total strand count, α_{Cu} is the electrical conductivity of copper, I is the RMS current, S is the cross-sectional area, μ_0 is the vacuum permeability, and μ_{Cu} is the relative permeability of copper. The resistivity of copper windings is characterized by the temperature coefficient $k_{\mathrm{Cu}} = 0.0039$. Then, the copper loss power P_{cu} is given by (3). Here, T is the operating temperature,

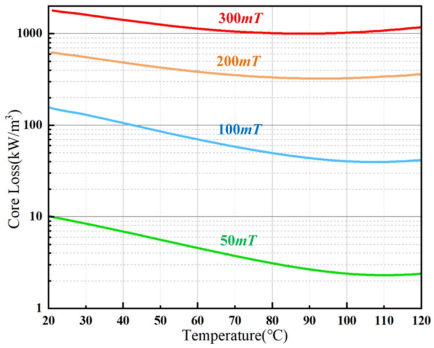

Fig. 4. Core Loss versus temperature characteristics of PC95 under different magnetic flux densities at 85 kHz.

T_0 is the reference temperature, and α_0 is the conductivity of copper at T_0

$$P_{cu} = \frac{I^2[k_{Cu}(T-T_0)+1]}{\alpha_0} \cdot \left[\sum_{i=1}^{N} \frac{2r_i}{r_s^2 n_0} + \frac{n_0 \pi \gamma^4}{4I^2 S} \int_V H^2(x,y,z)dv\right]. \quad (3)$$

2) Ferrite Core: The magnetic core material enhances energy transfer efficiency due to its high magnetic permeability. Based on the Bertotti loss separation model [33], [34], the core loss density P_{Core} under sinusoidal excitation consists of three components: hysteresis loss P_h, eddy current loss P_e, and excess loss P_{ex}. It is further expressed as

$$Pcore = P_h + P_e + P_{ex} = K_h f B_m^{\beta} + K_e f^2 B_m^2 + K_{ex} f^{1.5} B_m^{1.5}. \quad (4)$$

Here, K_h is the hysteresis loss coefficient, K_e is the eddy current loss coefficient, K_{ex} is the excess loss coefficient, B_m is the peak magnetic flux density, β is the Steinmetz exponent. For nonsinusoidal excitation, Fourier decomposition is applied to extract harmonic components for superposed loss estimation. Fig. 4 shows the variation of per-unit-volume core losses of PC95 material at 85 kHz when temperature and magnetic flux density vary.

3) Shielding: Circular eddy currents are induced on the surface of metallic shielding under high-frequency alternating magnetic fields. These currents generate a magnetic field that opposes the incident field, significantly attenuating its penetration and causing Joule losses within the shield. At high frequencies, the skin effect becomes prominent, leading to an exponential decay of current density along the shield thickness

$$J(x) = J_0 e^{-\frac{x}{\delta(T)}}, \delta(T) = \frac{1}{\sqrt{\pi f \sigma(T) \mu(T)}}, \mu(T) = \mu_0 \mu_{Al}(T). \quad (5)$$

The skin depth $\delta(T)$ is explicitly dependent on both the electrical conductivity $\sigma(T)$ and magnetic permeability $\mu(T)$, which vary with temperature. Aluminium is widely adopted for magnetic shielding owing to its high electrical conductivity, low density, and cost efficiency. Its resistivity is characterized by

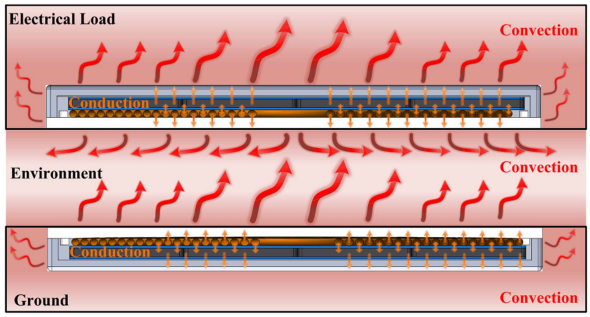

Fig. 5. Heat dissipation path in the WPT.

TABLE III
MATERIAL THERMAL PARAMETERS OF THE WCS

Component	Thermal Conductivity (W/m·K)	Specific Heat (J/Kg·℃)
Coil	400	385
Core	4.0	850
Shielding	230	900
Thermal grease	5	1300
Protective Housing	0.2	1600
Insulation Layer	0.2	1300
Coil Former	0.2	1900

the temperature coefficient $k_{\text{Al}} = 0.0043$. For a sinusoidally varying magnetic field perpendicular to the plate surface, the eddy current loss power density per unit area is given by (6). Here, σ_0 represents the electrical conductivity of aluminium at the reference temperature T_0

$$P_{Al} = \frac{B_{\text{rms}}^2}{\mu(T)^2} \cdot \sqrt{\frac{\pi f \mu(T)}{\sigma(T)}}, \sigma(T) = \frac{\sigma_0}{1 + k_{Al}(T - T_0)}. \quad (6)$$

The losses of all components are ultimately converted into thermal energy. Hence, analyzing the heat conduction process with the magnetic coupler and convection to the external environment is essential for elucidating the mechanism behind the rise in temperature.

D. Heat Dissipation Path

As illustrated in Fig. 5, heat transfer occurs through two main pathways: internal conduction between components and external convection to the environment.

1) Conduction: Electromagnetic losses in the coils, cores, and shielding generate distributed heat sources, producing pronounced temperature gradients in both axial and radial directions. To characterize this behavior, the heat transfer within each solid domain is modeled by the spatially varying transient Fourier equation

$$\rho_i c_i \frac{\partial T_i}{\partial t} = \nabla \cdot (\lambda_i \nabla T_i) + q_{em,i}. \quad (7)$$

Here, ρ_i, c_i, and λ_i denote the density, specific heat, and thermal conductivity of the ith component, and $q_{\text{em},i}$ represents the volumetric electromagnetic loss power. The material properties are given in Table III.

The ferrite core can be approximated as a one-dimensional medium with a uniform internal heat source to analyze the internal heat transfer further. The governing steady-state equation is expressed as (8). Its analytical solution gives the parabolic temperature distribution, as given by (9)

$$\frac{\partial^2 T}{\partial x^2} + \frac{q_{em}}{\lambda} = 0 \tag{8}$$

$$T(x) = -\frac{q_{\text{em}}}{2\lambda}x^2 + \left(\frac{T_{\text{shield}} - T_{\text{coil}}}{\delta} + \frac{q_{\text{em}}\delta}{2\lambda}\right)x + T_{\text{coil}} \tag{9}$$

where δ represents the thickness of the magnetic core, T_{coil} and T_{shield} denote the temperatures at the coil–core and core–shield interfaces, respectively. The heat conduction follows a radial path for the winding region due to its cylindrical geometry. The steady-state conduction equation in cylindrical coordinates is given by (10). It further leads to the following temperature distribution:

$$\frac{1}{r}\frac{d}{dr}\left(d\frac{dT}{dr}\right) + \frac{q_{\text{em}}}{\lambda} = 0. \tag{10}$$

This relationship explains the localized heating in the inner winding regions, where heat accumulation is most pronounced.

2) Convection: The magnetic coupler operates inside an enclosed device environment with minimal external forced airflow. Under such conditions, natural convection becomes the dominant cooling mechanism for dissipating the internally generated electromagnetic heat. The entire magnetic coupling assembly is encapsulated within a geometrically symmetric, rectangular protective enclosure, consisting of a top cover plate, a bottom base plate, and four sidewalls. Each of these six surfaces exhibits distinct thermal boundary characteristics due to differences in orientation and airflow accessibility, as shown in Fig. 5. All surfaces obey Newton's law of cooling

$$q_{\text{conv}} = Ah(T_s - T_{\text{env}}). \tag{11}$$

Here, q_{conv} is the heat flux, A is the effective surface area exposed to air convection, h is the heat transfer coefficient, T_s is the surface temperature, and T_{env} is the ambient temperature. Slight deviations in the calculated convection coefficients may lead to noticeable discrepancies in the predicted rise in surface temperature. The top horizontal surface, exposed to free air, constitutes the primary heat dissipation path. Its convection coefficient is estimated using the heated horizontal plate facing upwards model through the dimensionless Nusselt number Nu

$$h_{\text{top}} = \frac{N_{u\text{top}} \cdot k_{\text{air}}}{L_{\text{top}}}$$

$$N_{u\text{top}} = 0.54 \cdot R_{a\text{top}}{}^{\frac{1}{4}}, R_a = \frac{g\beta(T_s - T_{\text{env}})L^3}{va}. \tag{12}$$

Here, k_{air} is the thermal conductivity of air, L is the characteristic length, g is gravitational acceleration, β is the thermal expansion coefficient of air, ν is the kinematic viscosity, and a is the thermal diffusivity. The bottom surface of the protective enclosure experiences restricted airflow, resulting in weak natural convection and insufficient heat dissipation efficiency. The four side surfaces are treated as independent vertical plates, exhibiting moderate convection capability typically superior to the bottom surface but slightly inferior to the top surface. The following empirical correlation approximates its convection coefficient:

$$h_{\text{bottom}} \approx 0.27 R_{a\text{bottom}}{}^{\frac{1}{4}} \frac{k_{\text{air}}}{L_{\text{bottom}}}$$

$$h_{\text{side}} \approx 0.59 R_{a\text{side}}{}^{\frac{1}{4}} \frac{k_{\text{air}}}{L_{\text{side}}}. \tag{13}$$

The calculated Rayleigh numbers, Nusselt numbers, and corresponding convection coefficients for the air-exposed surfaces are given in Table IV. This model captures the heat dissipation heterogeneity inherent in enclosure geometry and establishes a foundation for setting thermal simulation boundary conditions.

TABLE IV
NATURAL CONVECTION PARAMETERS

Surface	Top	Bottom	Side
L (m)	0.0575	0.0575	0.02
R_a	$2.02 \times 10^4 \Delta T$	$2.02 \times 10^4 \Delta T$	$8.49 \times 10^2 \Delta T$
N_u	$0.54 \times (2.02 \times 10^4 \Delta T)^{1/4}$	$0.27 \times (2.02 \times 10^4 \Delta T)^{1/4}$	$0.59 \times (8.49 \times 10^2 \Delta T)^{1/4}$
h (W/m²·K)	$2.9\Delta T^{1/4}$	$1.45\Delta T^{1/4}$	$4.14\Delta T^{1/4}$

TABLE V
PREDICTION PERFORMANCE METRICS

Component	R^2	RMSE	RPD
Rxa-Copper	0.9933	1.4798	5.5703
Rxb-Core	0.9930	1.4725	5.51396
Rxc-Shielding	0.9920	1.5178	4.8608
Txa-Copper	0.9873	2.3851	5.5287
Txb-Core	0.9850	2.7597	5.4956
Txc-Shielding	0.9830	2.9843	5.4329

E. Thermal Model of the WCS

Power loss and thermal behavior in magnetic couplers are strongly coupled. Temperature influences the electromagnetic parameters, thereby affecting heat generation. Unidirectional models neglect these feedback effects, resulting in biased predictions under dynamic conditions. Thus, a bidirectional electromagnetic-thermal coupling model is established to capture these interactions and ensure accurate temperature prediction under varying operating scenarios.

The mutual inductance-based electromagnetic coupling is first solved to compute initial power losses. Subsequently, these loss densities are mapped as transient heat sources for thermal analysis. Iterative feedback of temperature-dependent material parameters refines the electromagnetic solution until steady-state convergence is achieved. The electromagnetic-thermal bidirectional coupling simulation is systematically illustrated in Fig. 6.

III. OPTIMAL FEATURE PARAMETER SCREENING

A. Generation of Multicondition Dataset

As Section II indicated, spatial offset and air gap variations directly alter the mutual inductance, indirectly leading to power transfer fluctuations. Power variations induce changes in power loss, thereby triggering distinct heat generation. To ensure a stable power supply on the load side, the WCS employs a constant

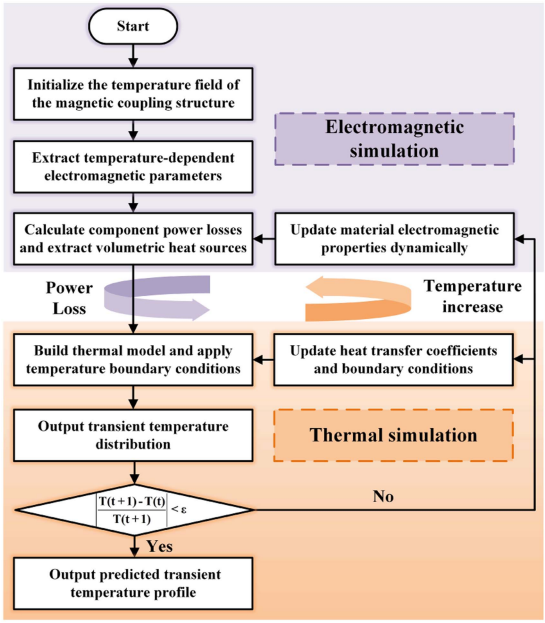

Fig. 6. Coupled electromagnetic-thermal bidirectional coupling simulation process.

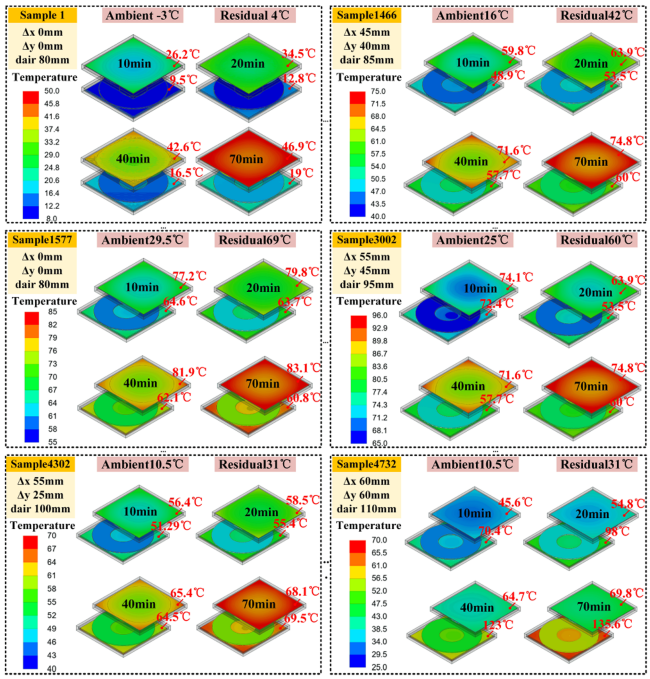

Fig. 7. Dataset encompassing multivariable operating conditions.

power control strategy, maintaining stable output power at the receiver under diverse operating conditions. Under this control scheme, despite significant variations in mutual inductance, the voltage and current changes at the receiver coil are relatively small, exerting a limited influence on the temperature rise.

In sequential charging cycles, magnetic couplers may not fully cool down after prolonged operation, resulting in residual heat at the next startup. This "residual heat effect" further superimposes on the standard heating, impacting the temperature rise process. Considering the WCS are often deployed outdoors, high summer temperatures reduce the system's heat dissipation efficiency, causing a more pronounced temperature rise. In contrast, during winter, low ambient temperatures facilitate rapid heat release, relatively improving the thermal tolerance of magnetic couplers.

Based on the above analysis, a comprehensive temperature prediction dataset was established to represent the WCSs coupled electromagnetic–thermal behavior under diverse and realistic conditions. The dataset covers multivariable operating scenarios, including ambient temperature variation, coil misalignment, air-gap fluctuation, and continuous charging cycles, resulting in a total of 4732 samples, as illustrated in Fig. 7. Each sample corresponds to a distinct spatial, electrical, and thermal configuration generated through deterministic electromagnetic–thermal coupling simulations, ensuring complete coverage of physically meaningful operating states. It provides a physically comprehensive and statistically balanced foundation for subsequent feature screening and model training, minimizing bias toward any specific operating condition.

B. Feature Selection Via Random Forest Algorithm

Key input features must be selected before constructing the prediction model to improve efficiency and accuracy. In this

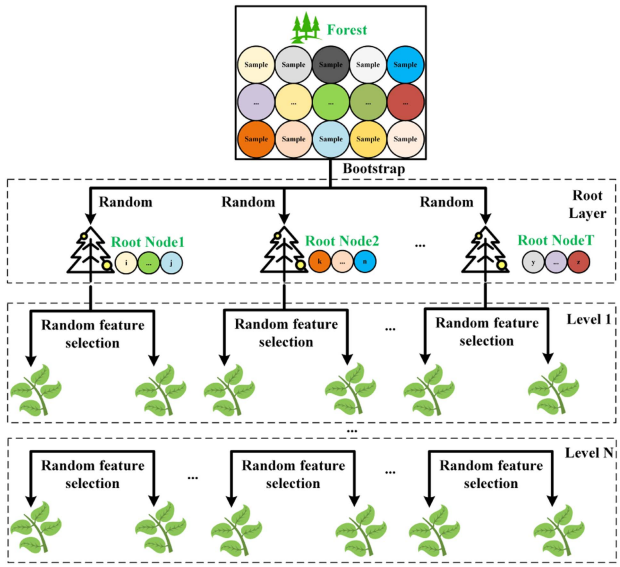

Fig. 8. Training process of random forest.

article, the Random Forest algorithm incorporates multitime and multioutput analysis to capture the evolving influence of the input variables throughout continuous charging. This refinement allows the LSTM model in Section IV to operate on a physically meaningful and dynamically optimized input set, effectively reducing redundancy, training time, and overfitting risk.

The training process of the random forest model involves two stages of controlled randomness, as illustrated in Fig. 8. In the first stage, bootstrap sampling is applied within the dataset to construct multiple sample subsets. Each subset corresponds to a different combination of electromagnetic and thermal operating

conditions and is used to train an independent regression tree. In the second stage, during the node-splitting process of each regression tree, a subset of input variables is randomly selected from all available features to determine the optimal splitting criterion. This strategy ensures that feature importance is evaluated from multiple physical perspectives, preventing dominance by any single variable.

In this article, the input features include ambient temperature, residual temperature, horizontal and vertical offset of the receiver, air gap height, transmitter coil current and voltage, and receiver coil current and voltage, totaling nine variables. The corresponding output target is the temperature variation trend of key components in the magnetic coupler over a future period under the given operating conditions.

During the node splitting process, random forest evaluates multiple potential numerical split points for each currently selected feature, calculating the resulting change in prediction error. Each split divides the samples at the current node into left and right subsets, and their respective mean squared errors (MSEs) are computed. The total post-split error is the weighted average of the errors of the two subsets. The algorithm selects the "feature–split point" combination that minimizes the weighted error as the optimal splitting criterion for the current node. The formula for calculating the total weighted MSE is as follows:

$$\mathrm{MSE}_L = \frac{1}{n_L}\sum_{i\in D_L}(y_i-\bar{y}_L)^2, \mathrm{MSE}_R = \frac{1}{n_R}\sum_{i\in D_R}(y_i-\bar{y}_R)^2$$

$$\mathrm{MSE}_{\mathrm{split}} = \frac{n_L}{n}\cdot\mathrm{MSE}_L + \frac{n_R}{n}\cdot\mathrm{MSE}_R. \quad (14)$$

Here, y_i denotes the actual temperature of the ith sample, $\bar{y}_L$ and $\bar{y}_R$ represent the predicted mean temperatures of the left and right subsets, n_L, n_R, and n are the sample counts of the left subset, proper subset, and current node, respectively. If the total weighted MSE after a split is smaller than any other split point, the node is split at that point.

To evaluate the contribution of each input feature to the temperature prediction task, the mean decrease impurity (MDI) method is employed to quantify feature importance. MDI statistically measures the reduction in MSE brought by each feature when used for node splitting in the random forest, thereby reflecting its degree of influence within the overall model. The feature selection process adopted in this article is illustrated in Fig. 9.

If a feature x_j is used to split a node k in a regression tree, this splitting causes a reduction in the prediction error at the current node. The reduction amount of this error is denoted as $\Delta\mathrm{MSE}(x_j, k)$. The importance score of feature x_j across the entire random forest can be obtained by summing the error reductions from all node splits used in all decision trees. The calculation expression is as follows:

$$\mathrm{Importance}(x_j) = \sum_{t=1}^{T\mathrm{total}}\sum_{n\in N_t(x_j)} \triangle\ \mathrm{MSE}(x_j,k). \quad (15)$$

Here, T_{total} is the number of decision trees in the random forest, and $N_t(x_j)$ represents the set of all nodes in the tth tree where feature x_j is used for splitting. By statistically aggregating the error contributions of this feature across all nodes and trees, its relative importance in the entire model is determined.

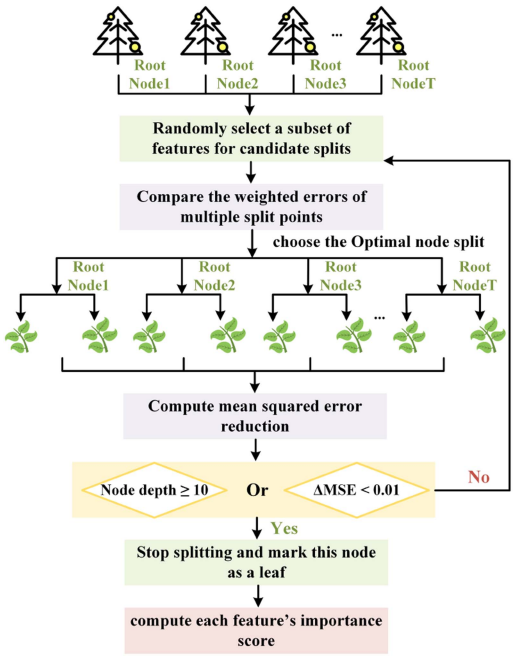

Fig. 9. Random forest feature importance evaluation flowchart.

Fig. 10 displays the importance distribution of key input features across six critical temperature measurement points at different prediction timesteps. The proposed random forest model configuration enables dynamic tracking of feature relevance over time, revealing the temporal evolution of thermal sensitivity.

During the short-term prediction phase, the residual temperature is critical at all measurement points, with dominant significance particularly in the coil regions. This indicates that residual thermal effects constitute the primary factor influencing temperature variations during initial system startup, with the model relying more heavily on historical thermal states to predict initial temperature rise trends.

As prediction duration extends to 20–40 min, the feature weight of ambient temperature progressively increases, becoming dominant at multiple receiver-side measurement points. This reflects the growing influence of external environments on heat dissipation efficiency during mid-term stages. Simultaneously, the transmitter coil voltage and current exhibit predictive contributions at partial hotspot locations, indicating that fluctuations in supply parameters indirectly regulate mid-term temperature rise processes.

During the long-term prediction phases, the influence of residual temperature gradually diminishes while the importance of ambient temperature remains high. The significance of transmitter-side electrical parameters increases further at localized measurement points, particularly becoming the dominant influencing factor in transmitter-side hotspot regions. It is worth noting that the experimental dataset employed a constant power control strategy during the simulation. Consequently, although coil voltage and current represent the modelling process, their

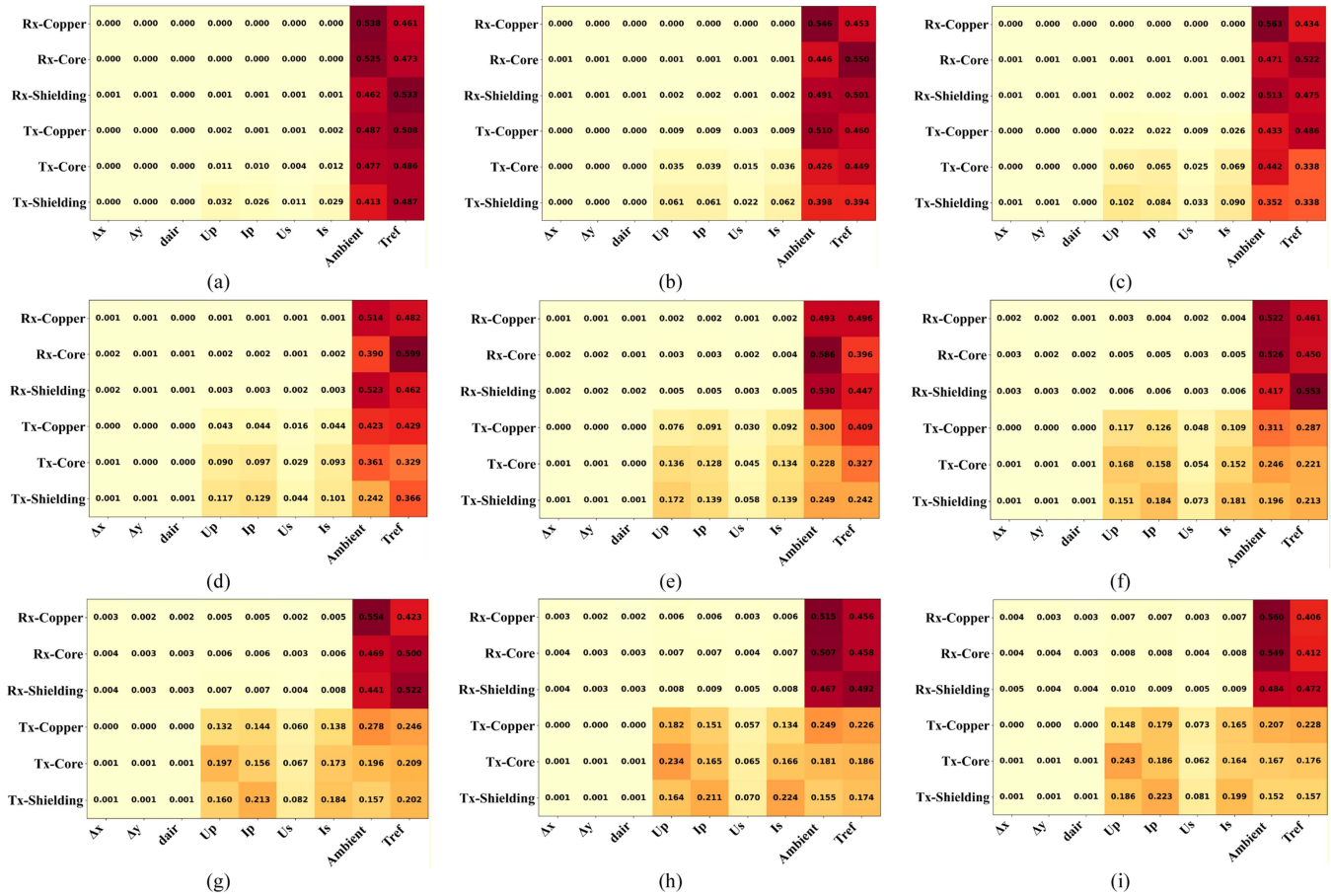

Fig. 10. Feature importance heatmaps at different forecast time steps. (a) 5 min. (b) 10 min. (c) 15 min. (d) 20 min.(e) 30 min. (f) 40 min. (g) 50 min. (h) 60 min. (i) 70 min.

direct impact on temperature variations is limited; if the system operates in open-loop mode, temperature rise would exhibit greater sensitivity to current fluctuations.

Based on the feature importance evaluation and the high linear correlation between the coil voltages and currents at both the transmitter and receiver sides, this article selects residual temperature, ambient temperature, and coil currents as input features for the LSTM prediction model construction and training. Coil voltages and spatial offset variables were removed due to high redundancy or indirect influence, while the retained features offer strong physical interpretability and direct relevance to thermal behavior. This approach strikes a balance between model accuracy and computational efficiency.

C. Data Preprocessing

The full dataset was randomly shuffled using a fixed random seed to eliminate temporal or condition-based clustering, ensuring generalization and avoiding prediction bias under specific working conditions. All samples were segmented into nonoverlapping sequences of fixed time length and then divided into 90% for training and 10% for validation. The remaining samples were extracted sequentially from the tail of the dataset to form the test set.

IV. Temperature Prediction Model Integrating LSTM With Temporal Self-Attention Mechanism

A. LSTM Deep Neural Network

Compared to the traditional recurrent neural networks, the LSTM network mitigates the vanishing and exploding gradient issues while training long-sequence data by introducing gating mechanisms, significantly enhancing model stability and accuracy in handling long-term dependencies [35]. The LSTM network holds temperature prediction advantages and has evolved into an established model. However, unlike conventional LSTM frameworks developed for smooth or stationary data, the proposed network in this study was specifically adapted to the nonstationary, strongly coupled, and thermally accumulative behavior of WCSs.

The LSTM unit structure is illustrated in Fig. 11. The Input Gate controls the degree of influence of the current input features, X_t, on the Cell State. To determine whether current input features significantly impact the temperature rise process, thereby deciding whether such information should be incorporated into the cell state

$$I_t = \sigma(W_{xi}X_t + W_{hi}H_{t-1} + b_i). \tag{16}$$

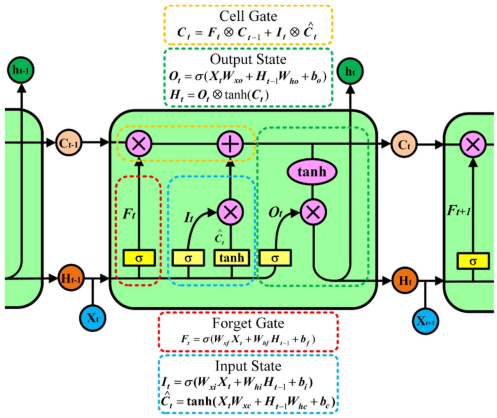

Fig. 11. Structure of LSTM.

Here, σ denotes the sigmoid activation function regulating the memorization degree of current information; W_{xi} and W_{hi} are weight matrices; b_i is the bias term, and H_{t-1} represents the hidden state at the previous time step. The forget gate evaluates the retention value of information within the historical cell state C_{t-1}.

The forget gate selectively memorizes or discards historical thermal state information by adjusting the retention ratio of historical data

$$F_t = \sigma(W_{xf}X_t + W_{hf}H_{t-1} + b_f). \tag{17}$$

Subsequently, the candidate cell state generates new candidate memory information $\hat{C}_t$, collaborating with the input gate to determine current memory state updates. In this step, the network introduces the tan*h* nonlinear activation function to capture complex nonlinear characteristics in magnetic coupler temperature variations, such as nonuniform thermal effects caused by air gap variations, and position offsets

$$\hat{C}_t = \tan h(W_{xc}X_t + W_{hc}H_{t-1} + b_c). \tag{18}$$

After joint regulation by the input gate and forget gate, the cell state C_t is updated as

$$C_t = F_t \otimes C_{t-1} + I_t \otimes \hat{C}_t. \tag{19}$$

The cell state update process explicitly expresses the selective retention of historical information and the integration of current operational data, ensuring that the model captures long-term residual heat accumulation and rapid temperature responses caused by misalignment-induced electrical fluctuations. Finally, the output gate controls the extraction and output of hidden state H_t, selectively transmitting current cell state information to the prediction layer to generate temperature predictions at multiple key measurement points in the magnetic coupler structure

$$\begin{aligned} O_t &= \sigma(W_{xo}X_t + W_{ho}H_{t-1} + b_o) \\ H_t &= O_t \otimes \tan h(C_t). \end{aligned} \tag{20}$$

The hidden state H_t integrates influences from historical states and current operating conditions, serving as the final output for predicting the hotspot temperature trend at the current timestep. The LSTM network effectively captures intrinsic thermal inertia and long-term memory effects through the synergistic operation of these gating mechanisms.

B. Integration of Temporal Self-Attention Mechanism

Traditional LSTM models assign identical importance to hidden states generated at all timesteps when processing sequence prediction tasks. This approach neglects the differential contributions of individual timesteps to the final prediction outcome. In temperature prediction, the temporal evolution of hotspot temperatures exhibits distinct phase characteristics, with forecasts during different periods exerting varying influences on final temperature trends. Uniformly weighting outputs across all timesteps may obscure critical transitional information, reducing model sensitivity to temperature dynamics and compromising prediction accuracy.

To address these limitations, a temporal self-attention mechanism was incorporated into the output layer of the LSTM network. This module dynamically evaluates the physical significance of each timestep by weighting hidden states according to their contribution to subsequent heat generation. First, the LSTM layer encodes input sequences into a series of hidden state vectors *h*, each representing temporal information at a step. Subsequently, the temporal self-attention mechanism assigns scores to each hidden state to quantify its importance to the final prediction. The attention scoring function is typically implemented through a trainable feedforward neural network, formally defined as

$$e_t = v_a^{\top} \tan h(W_a h_t + b_a). \tag{21}$$

Here, W_a is the weight matrix, v_a is the attention vector, b_a is the bias term, and e_t denotes the attention score at each timestep. This score reflects the relative importance of that timestep to the current prediction output. Subsequently, all timestep scores are normalized via the Softmax function to obtain attention weights α_t per timestep, values range between 0 and 1, with summed weights equal to 1

$$\alpha_t = \frac{\exp(e_t)}{\sum_{k=1}^{T} \exp(e_k)}. \tag{22}$$

This weight coefficient α_t represents the contribution of the hidden state at timestep *t* to the final prediction outcome. A larger weight indicates a more significant influence of that timestep's hidden state on the prediction. Finally, all hidden state vectors undergo weighted summation according to the computed attention weights to obtain the global context vector v_C, which integrates fast transient responses and slow diffusion-driven heating behaviors, yielding a physically interpretable representation of the temperature evolution:

$$vC = \sum_{t=1}^{T} \alpha_t h_t. \tag{23}$$

The v_C integrates information from all critical moments, embodying global temporal dependencies. It is fed into the output layer to predict temperature variation trends at multiple

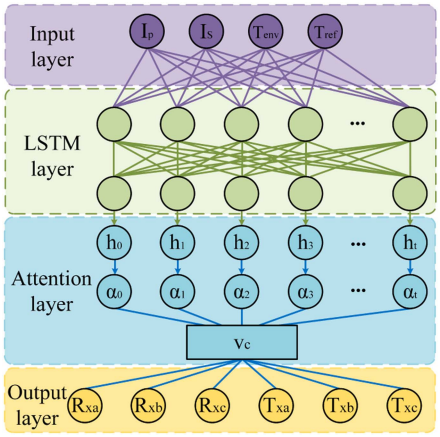

Fig. 12. Temperature prediction network architecture diagram based on LSTM integrated with temporal self-attention mechanism.

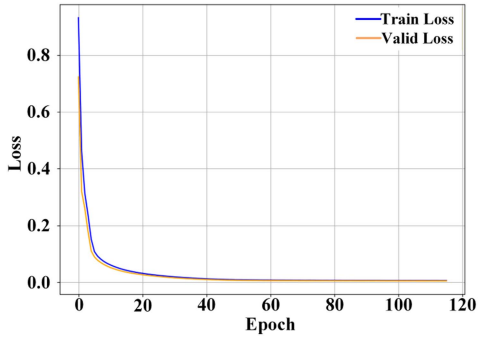

Fig. 13. Loss convergence curves during model training.

measurement points in the magnetic coupler structure for future timesteps. Fig. 12 illustrates the proposed network architecture integrating LSTM with a temporal self-attention mechanism.

V. Experimental Verification

A. Model Evaluation

This section conducts an in-depth analysis of three aspects: convergence characteristics, prediction accuracy, and generalization capability, to comprehensively evaluate the performance of the proposed LSTM model integrated with a temporal self-attention mechanism for multipoint temperature prediction in magnetic couplers.

Fig. 13 shows the loss convergence curves during training. The blue curve denotes training set loss, while the orange curve represents validation set loss. As the number of training epochs increases, both loss values decrease rapidly and stabilize after approximately 80 epochs, with the final residuals converging to below 10^{-3}. This indicates the model achieves rapid and stable convergence while effectively avoiding overfitting. Furthermore, the validation loss remains low, demonstrating robust generalisation capability for prediction tasks across different data distributions.

Table V lists R^2, RMSE, and RPD metrics at six key prediction points in the test set for quantitative assessment of prediction accuracy and reliability in magnetic coupler hotspot temperature forecasting. All measurement points exhibit R^2 exceeding 0.98, indicating excellent fitting performance; RMSE values remain below 3, reflecting minimal prediction errors; RPD values all exceed 4.8, substantially higher than the reliability threshold of 3.0 for conventional models. This confirms high prediction stability, making it suitable for engineering applications.

Scatter plots are commonly used graphical tools for intuitively demonstrating relationships between actual and predicted values, effectively reflecting the performance of model fitting. Fig. 14 compares the prediction results of the LSTM model integrated with a temporal self-attention mechanism to those of conventional LSTM models at six critical temperature measurement points across different timesteps. Each scatter point represents the correspondence between the actual and predicted temperatures at a measurement point for the current timestep, where $y = x$ indicates perfect prediction alignment under ideal conditions.

The LSTM model with an integrated temporal self-attention mechanism demonstrates higher fitting accuracy and stability across all timesteps. Particularly during the mid-to-long-term prediction phase, predicted values at nearly all measurement points closely align with the actual values, exhibiting strong linear fitting relationships.

In contrast, the conventional LSTM model exhibits relatively scattered prediction point distributions at short timesteps, with significant deviations observed at partial measurement points, indicating noticeable volatility and error accumulation trends. During long-term prediction phases, prediction point deviations intensify, where some measurement points show apparent underestimation or overestimation of actual temperatures. This reflects inherent limitations of conventional LSTM models in capturing long-term temporal dependencies and critical feature information. This indicates that with integrated temporal self-attention, the model more effectively identifies critical moments of temperature rise variations during thermal evolution processes, enhances modelling capability for complex temperature dynamics, and achieves accurate predictions of dynamic temperature trends.

Experimental results confirm that the proposed improved model demonstrates superior engineering applicability and practical application potential for temperature prediction tasks in magnetic couplers.

B. Experimental Prototype

As shown in Fig. 15, an experimental prototype was built according to the parameters in Table II to validate the adaptability and effectiveness of the proposed prediction model in a practical WCS. The controller employed an STM32F405RGT6 microcontroller chip. The primary circuit adopts a full-bridge inverter structure composed of four N-channel power MOSFETs (C2M0040120D), driven by four single-channel isolated gate drivers (1EDI60N12AF). The SS compensation circuit utilizes low-power film capacitors, while the rectification section consists of four diodes (STTH30L06CG). The output is stabilized

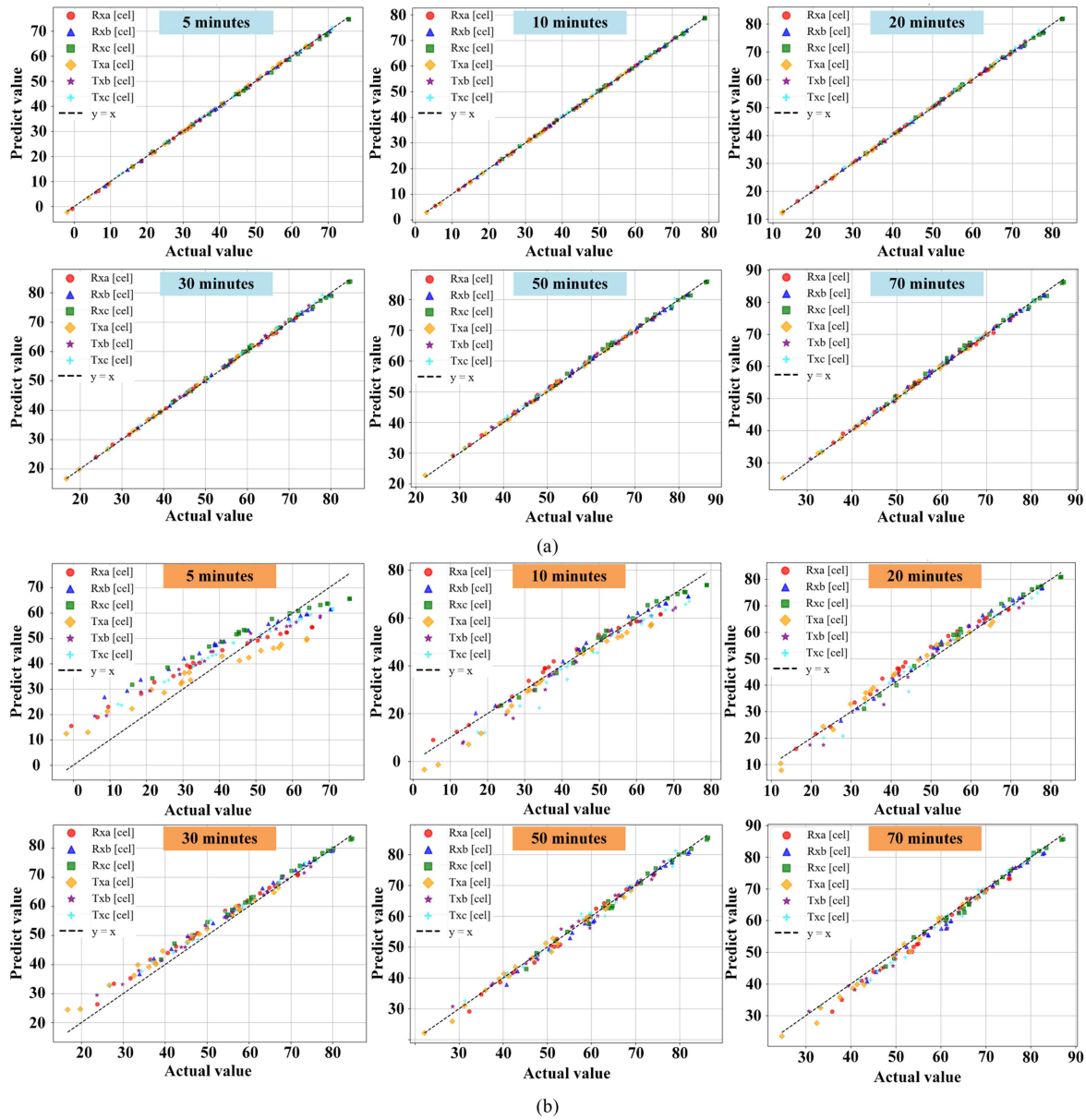

Fig. 14. Scatter plots of predicted versus actual temperatures at different prediction time steps for both models. (a) LSTM integration of temporal self-attention mechanism. (b) Long short-term memory.

through nonpolar filtering capacitors. System dc power is supplied by a KEYSIGHT N8949A adjustable source, with signal acquisition performed using a SIGLENT SDS2204X digital oscilloscope.

Six fluorescent fibre optic temperature sensors were deployed at key heating locations for multipoint temperature monitoring. Temperature measurement employs a continuous sampling strategy at 2-s intervals. At the same time, thermal distribution images are captured using a visual infrared thermometer (FLUKE VT-04A) to validate the consistency between simulated temperature fields and measured temperature rises.

Fig. 16 shows experimentally captured voltage and current waveforms at the transmitter and receiver sides. Here, u_i and u_e represent high-frequency voltages at the inverter output and rectifier input terminals, respectively, while i_p and i_s denote current waveforms in the transmitter and receiver coils. The waveforms exhibit overall stability with no observable harmonic distortion, validating system power transfer stability.

Under an ambient temperature of 25.5°C, infrared thermal imaging continuously monitored temperatures at the top surface of the receiver and transmitter sides. As shown in Fig. 17, the transmitter-side temperature distributions exhibit consistent spatial patterns between simulation and infrared measurements. The predicted hotspot regions correspond well to the coil windings and ferrite core, confirming that the electromagnetic–thermal coupling accurately captures the localized loss distribution. Similarly, on the receiver side, the simulated and measured results show comparable temperature gradients and hotspot evolution trends. The results demonstrate strong agreement between the simulated and experimental temperature fields, thereby validating the fidelity of the thermal modeling.

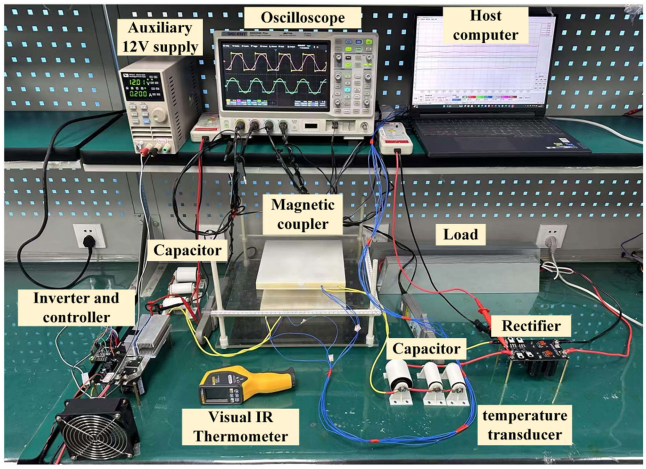

Fig. 15. Experimental prototype of the designed WCS.

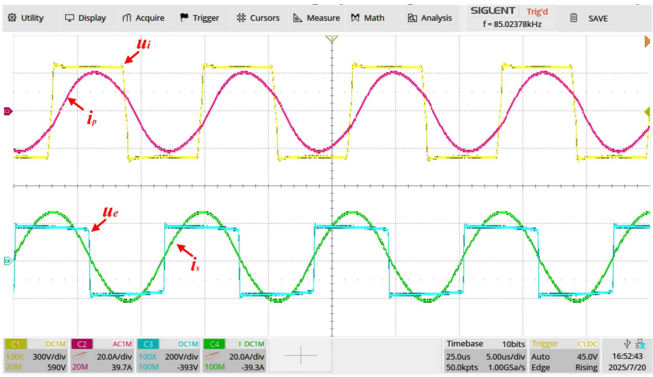

Fig. 16. Waveform of the WCS.

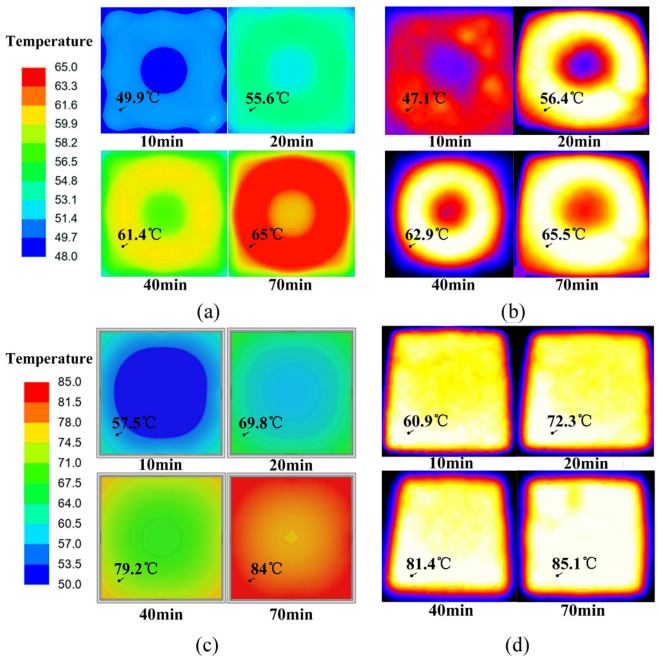

Fig. 17. Thermal temperature distribution at four typical times. (a) Transmitter-side. (b) Transmitter-side. (c) Receiver side. (d) Receiver side.

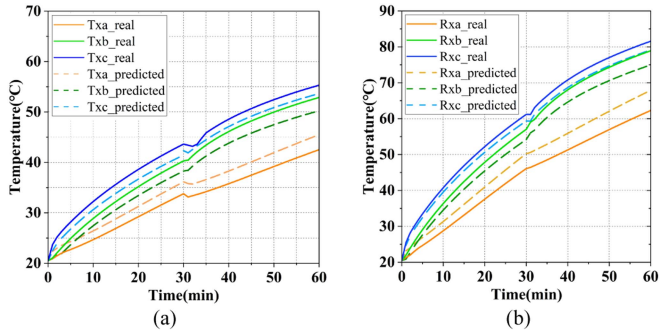

Fig. 18. Comparison of measured and predicted temperature curves. (a) Transmitter-side components. (b) Receiver-side components.

C. Comparative Verification of Prediction and Measured Results

To further validate the accuracy and adaptability of the proposed LSTM model, experimental data under typical operating conditions were compared. The ambient temperature was set at 20.5 °C. Test conditions were: coil spatial offsets $\Delta x = 10$ mm, $\Delta y = 25$ mm with 95 mm air gap; subsequently changed to $\Delta x = 35$ mm, $\Delta y = 25$ mm with 85 mm air gap. These conditions simulate typical temperature rise processes caused by transformer misalignment and structural variations during continuous charging.

Temperature variation curves were collected at six key measurement points throughout the charging cycle. The initial operation under one offset condition lasted 30 min, followed by another 30-min operation under modified conditions, totaling 60 min. Fig. 18 compares the proper temperature curves recorded by sensors with predicted temperatures. The solid lines represent measured values, while the dashed lines denote model predictions.

The proposed model demonstrates favorable prediction consistency across all key measurement points, with a mean error of 5.7%. Specifically for the shielding and core regions, mean errors are 5.1% and 6%, respectively. These regions exhibit excellent overall trend fitting, validating the accurate capture capability for mid-to-long-term temperature rise evolution. Coil predictions show slightly higher errors, with a mean error of 8%, potentially attributable to minor positional deviations in sensor placement or non-uniform thermal conductivity of adhesive materials. The remaining discrepancies mainly arise from insulation-induced heat transfer delay and the thermal inertia of real components, where temperature gradients and response lags are more pronounced.

VI. Conclusion

This article proposes a rapid, real-time hotspot temperature prediction method for magnetic couplers in WCS. First, a model for loss and thermal dissipation in magnetic couplers was established. Electromagnetic-thermal bidirectional coupling simulations were performed using the FEM, obtaining temperature distribution data under multicondition operations. Subsequently, the random forest algorithm analyzed and screened key input

features that significantly influenced temperature predictions. Then, an LSTM temperature prediction model integrated with a temporal self-attention mechanism was developed. The model exhibits exceptional prediction accuracy and generalization capability in validation tests, with R^2 exceeding 0.98 at all measurement points, RMSE below 3, and RPD above 4.8. Finally, a 3.3 kW experiment validated the proposed method. The overall mean prediction error across measurement points was approximately 5.7%, with shield and core regions showing mean errors of 5.1% and 6% respectively, and the coil region averaging 8%. The proposed real-time hotspot temperature prediction method enables rapid temperature forecasting for magnetic couplers. It provides reliable foundations for dynamic power adjustment and real-time thermal safety control in WCS, demonstrating strong engineering utility and application prospects.

REFERENCES

[1] A. Mostafa, Y. Wang, F. Lu, and H. Zhang, "Enhanced axial misalignment tolerance in a 10-kW autonomous underwater vehicle wireless charging system utilising a split solenoid coupler," *IEEE Trans. Power Electron.*, vol. 39, no. 10, pp. 12041–12046, Oct. 2024.

[2] Z. Shen, H. Zhou, R. Xie, Y. Zhuang, X. Mao, and Y. Zhang, "A strong offset-resistant electric vehicle wireless charging system based on dual decoupled receiving coils," *IEEE Trans. Ind. Electron.*, vol. 71, no. 11, pp. 15216–15219, Nov. 2024.

[3] H. Feng, R. Tavakoli, O. C. Onar, and Z. Pantic, "Advances in high-power wireless charging systems: Overview and design considerations," *IEEE Trans. Transp. Electrific.*, vol. 6, no. 3, pp. 886–919, Sep. 2020.

[4] M. Zhang, Z. Liu, and H. Su, "Robust adaptive output regulation for EV dynamic wireless charging system with sinusoidal disturbance of unknown frequency," *IEEE Trans. Ind. Electron.*, vol. 71, no. 7, pp. 7301–7311, Jul. 2024.

[5] J. Liu, Z. Liu, and H. Su, "Passivity-based PI control for receiver side of dynamic wireless charging system in electric vehicles," *IEEE Trans. Ind. Electron.*, vol. 69, no. 1, pp. 783–794, Jan. 2022.

[6] Y. Zhang, H. Zhou, R. Xie, X. Mao, X. Chen, and Z. Li, "A smooth-output dynamic wireless charging system for automated guided vehicles with dual-receiver magnetic coupler," *IEEE Trans. Power Electron.*, vol. 40, no. 4, pp. 4711–4715, Apr. 2025.

[7] K. Chen, Y. Ouyang, X. Yang, N. C. Cheung, E. K.-W. Cheng, and J. Pan, "A high-interoperability optimal frequency control method for the AGV dynamic wireless charging systems without communication," *IEEE Trans. Power Electron.*, vol. 39, no. 3, pp. 3797–3808, Mar. 2024.

[8] C. Cai, X. Liu, S. Wu, X. Chen, W. Chai, and S. Yang, "A misalignment tolerance and lightweight wireless charging system via reconfigurable capacitive coupling for unmanned aerial vehicle applications," *IEEE Trans. Power Electron.*, vol. 38, no. 1, pp. 22–26, Jan. 2023.

[9] S. Wu, C. Cai, X. Liu, W. Chai, and S. Yang, "Compact and free-positioning omnidirectional wireless power transfer system for unmanned aerial vehicle charging applications," *IEEE Trans. Power Electron.*, vol. 37, no. 8, pp. 8790–8794, Aug. 2022.

[10] S. Niu, H. Yu, S. Niu, and L. Jian, "Power loss analysis and thermal assessment on wireless electric vehicle charging technology: The over-temperature risk of ground assembly needs attention," *Appl. Energy*, vol. 275, Oct. 2020, Art. no. 115344.

[11] C. Xiao, S. Hao, D. Cheng, and C. Liao, "Safety enhancement by optimising frequency of implantable cardiac pacemaker wireless charging system," *IEEE Trans. Biomed. Circuits Syst.*, vol. 16, no. 3, pp. 372–383, Jun. 2022.

[12] D. Li, X. Wu, W. Gao, D. Luo, and J. Gao, "Coupler loss analysis of magnetically coupled resonant wireless power transfer system," *CES Trans. Elect. Machines Syst.*, vol. 7, no. 1, pp. 63–72, Mar. 2023.

[13] S. Kim et al., "Thermal evaluation of an inductive power transfer pad for charging electric vehicles," *IEEE Trans. Ind. Electron.*, vol. 69, no. 1, pp. 314–322, Jan. 2022.

[14] C. Liang et al., "Modeling and analysis of thermal characteristics of magnetic coupler for wireless electric vehicle charging system," *IEEE Access*, vol. 8, pp. 173177–173185, 2020.

[15] B. Zhang et al., "Multiobjective thermal optimization based on improved analytical thermal models of a 30-kW IPT system for EVs," *IEEE Trans. Transp. Electrific.*, vol. 9, no. 1, pp. 1910–1926, Mar. 2023.

[16] A. Delgado, L. Clavero, M. Vasic, P. Alou, M. Bakic, and T. Wijekoon, "3D thermal modeling of inductive power transfer coils based on basic thermal network for optimization analysis," in *Proc. IEEE Appl. Power Electron. Conf. Expo.*, 2023, pp. 3314–3321.

[17] D. Wang, J. Wei, H. Feng, and L. Ran, "A thermal black-box theory for scaling design of planar magnetic coils in wireless charging systems," *IEEE Trans. Power Electron.*, vol. 39, no. 7, pp. 8973–8984, Jul. 2024.

[18] N. Rogkas, E. Karampasakis, M. Fotopoulou, and D. Rakopoulo, "Assessment of heat transfer mechanisms of a novel high-frequency inductive power transfer system and coupled simulation using FEA," *Energy*, vol. 300, Aug. 2024, Art. no. 131530.

[19] V. Kindl, R. Pechanek, M. Zavrel, and T. Kavalir. P. Turjancia, "Inductive coupling system for electric scooter wireless charging: Electromagnetic design and thermal analysis," *Elect. Eng.*, vol. 102, pp. 3–12, Mar. 2020.

[20] M. Amirpour, S. Kim, M. P. Battley, P. Kelly, S. Bickerton, and G. Covic, "Coupled electromagnetic-thermal analysis of roadway inductive power transfer pads within a model pavement," *Appl. Thermal Eng.*, vol. 189, May 2021, Art. no. 116710.

[21] M. Mohammad, O. C. Onar, J. L. Pries, V. P. Galigekere, G.-J. Su, and J. Wilkins, "Thermal analysis of a 50 kW three-phase wireless charging system," in *Proc. IEEE Trans. Electrific. Conf. Expo*, 2021, pp. 1–6.

[22] J. Ma, Z. Li, Y. Liu, M. Ban, and W. Song, "Thermal analysis and optimization of the magnetic coupler for wireless charging system," *IEEE Trans. Power Electron.*, vol. 38, no. 12, pp. 16269–16280, Dec. 2023.

[23] J. I. Aizpurua, S. D. J. McArthur, B. G. Stewart, B. Lambert, J. G. Cross, and V. M. Catterson, "Adaptive power transformer lifetime predictions through machine learning and uncertainty modeling in nuclear power plants," *IEEE Trans. Ind. Electron.*, vol. 66, no. 6, pp. 4726–4737, Jun. 2019.

[24] L. Zhou et al., "A method for hotspot temperature prediction and thermal capacity estimation for traction transformers in high-speed railway based on genetic programming," *IEEE Trans. Transp. Electrific.*, vol. 5, no. 4, pp. 1319–1328, Dec. 2019.

[25] H. Wang et al., "A junction temperature monitoring method for IGBT modules based on turn-off voltage with convolutional neural networks," *IEEE Trans. Power Electron.*, vol. 38, no. 8, pp. 10313–10328, Aug. 2023.

[26] L. Li, J. Liu, M.-L. Tseng, and M. K. Lim, "Accuracy of IGBT junction temperature prediction: An improved sailfish algorithm to optimize support vector machine," *IEEE Trans. Power Electron.*, vol. 39, no. 6, pp. 6864–6876, Jun. 2024.

[27] G. Mengrong and L. Hongjian, "Research on temperature prediction of subway transformer based on LSTM," in *Proc. IEEE Int. Conf. Artif. Intell. Comput. Appl.*, 2022, pp. 555–558.

[28] Y. Sui, K. Yan, A. M. A. Abdo, H. Zhang, H. Liu, and H. Cong, "Prediction of transformer top oil temperature based on bayesian optimization and LSTM neural network," in *Proc. Int. Conf. Power Syst. Technol.*, 2023, pp. 1–5.

[29] C. Li, J. Chen, C. Xue, Z. Liu, and P. Davari, "Simultaneous multispot temperature prediction of traction transformer in urban rail transit using long short-term memory networks," *IEEE Trans. Transp. Electrific.*, vol. 9, no. 3, pp. 4552–4561, Sep. 2023.

[30] Z.-W. Du et al., "A time series characterization of IGBT junction temperature method based on LSTM network," *IEEE Trans. Power Electron.*, vol. 40, no. 1, pp. 2070–2085, Jan. 2025.

[31] N. Rasekh, S. Dabiri, N. Rasekh, M. Mirsalim, and M. Bahiraei, "Thermal analysis and electromagnetic characteristics of three single-sided flux pads for wireless power transfer," *J. Cleaner Prod.*, vol. 243, Jan. 2020, Art. no. 118561.

[32] S. Ehrlich, H. Rossmanith, M. Sauer, C. Joffe, and M. März, "Fast numerical power loss calculation for high-frequency Litz wires," *IEEE Trans. Power Electron.*, vol. 36, no. 2, pp. 2018–2032, Feb. 2021.

[33] Z. Li, W. Han, Z. Xin, Q. Liu, J. Chen, and P. C. Loh, "A review of magnetic core materials, core loss modeling and measurements in high-power high-frequency transformers," *CPSS Trans. Power Electron. Appl.*, vol. 7, no. 4, pp. 359–373, Dec. 2022.

[34] M. Mohammad, S. Choi, and M. E. Elbuluk, "Loss minimization design of ferrite core in a DD-coil-based high-power wireless charging system for electrical vehicle application," *IEEE Trans. Transp. Electrific.*, vol. 5, no. 4, pp. 957–967, Dec. 2019.

[35] K. Greff, R. K. Srivastava, J. Koutnìk, B. R. Steunebrink, and J. Schmidhuber, "LSTM: A search space Odyssey," *IEEE Trans. Neural Netw. Learn. Syst.*, vol. 28, no. 10, pp. 2222–2232, Oct. 2017.